Tailward flow of energetic neutral atoms observed at Mars

A. Galli,[1] P. Wurz,[1] E. Kallio,[2] A. Ekenbäck,[3] M. Holmström,[3] S. Barabash,[3] A. Grigoriev,[3] Y. Futaana,[3] M.-C. Fok,[4] and H. Gunell[5]

[1] The ASPERA-3 experiment on Mars Express provides the first measurements of energetic neutral atoms (ENAs) from Mars. These measurements are used to study the global structure of the interaction of the solar wind with the Martian atmosphere. In this study we describe the tailward ENA flow observed at the nightside of Mars. After characterizing energy spectra of hydrogen ENA signals, we present composite images of the ENA intensities and compare them to theoretical predictions (empirical and MHD models). We find that the tailward flow of hydrogen ENAs is mainly generated by shocked solar wind protons. Despite intensive search, no oxygen ENAs above the instrument threshold are detected. The results challenge existing plasma models and constrain the hydrogen exospheric densities and atmospheric hydrogen and oxygen loss rates at low solar activity.

Citation: Galli, A., P. Wurz, E. Kallio, A. Ekenbäck, M. Holmström, S. Barabash, A. Grigoriev, Y. Futaana, M.-C. Fok, and H. Gunell (2008), Tailward flow of energetic neutral atoms observed at Mars, *J. Geophys. Res.*, *113*, E12012, doi:10.1029/2008JE003139.

1. Introduction

[2] The Analyzer of Space Plasmas and Energetic Atoms, ASPERA-3, instrument consists of four different sensors [*Barabash et al.*, 2006]. For in situ plasma measurements there are the Ion Mass Analyzer (IMA) and the Electron Spectrometer (ELS). For remote sensing using energetic neutral atoms there are the Neutral Particle Imager (NPI) and the Neutral Particle Detector (NPD). NPI has a 360° × 5° instantaneous field-of-view with good angular resolution, but lacks the energy measurement and the particle identification. For a recent NPI analysis, see *Gunell et al.* [2006a]. NPD has a 180° × 6° instantaneous field-of-view with moderate angular resolution, but with energy measurement and mass identification. The present study is focused on the NPD data recorded at the nightside of Mars.

[3] In the last four years, the ASPERA-3 experiment on Mars Express has revealed many aspects of the plasma environment around Mars [*Barabash et al.*, 2007a]. A comprehensive summary of the first years of IMA and ELS observations of plasma boundaries, ion outflow, escape processes, influence of crustal magnetic fields and photoelectrons was given by *Dubinin et al.* [2006]; a statistical study of the plasma moments derived from IMA data were

presented by *Fränz et al.* [2006] (the proton and electron densities around Mars are shown in Figure 1). Ion escape rates were studied by *Barabash et al.* [2007a]; the chemical composition of escaping plasma was investigated by *Carlsson et al.* [2006].

[4] The interaction of the solar wind plasma with the planetary environment leads to the formation of two distinct boundaries. Figure 1 shows the electron and proton densities in the Mars environment with the two plasma boundaries (thin black lines) superimposed on the data with densities derived from ELS and IMA measurements, respectively [*Dubinin et al.*, 2006]. At the bow shock, the solar wind is slowed down to subsonic velocities, the magnetosheath between the bow shock and the inner plasma boundary is dominated by slow, heated up solar wind. The inner plasma boundary can either be defined as the boundary where the planetary ions start to outnumber the magnetosheath ions or as the boundary where the interplanetary magnetic field B_{IMF} piles up around the ionosphere. The two different concepts are equivalent [*Bößwetter et al.*, 2004]. In this paper we shall use the term "Induced Magnetosphere Boundary" (IMB) for the inner plasma boundary.

[5] The motivation for the energetic neutral atom (ENA) observations at Mars is to provide a global view of the interaction of the solar wind with the neutral atmosphere of Mars, a nonmagnetized planet, to complement the local plasma measurements. To fully interpret the ENA observations, a comparison with ENA models is needed.

[6] An ENA is the product of a charge exchange reaction between an energetic ion and a neutral atom. In the present study on ENA observations at Mars the energetic ions are typically solar wind protons and the neutrals are hydrogen atoms of the planetary exosphere. For a flow of monoenergetic hydrogen ions $j_p(r)$ that are neutralized along their
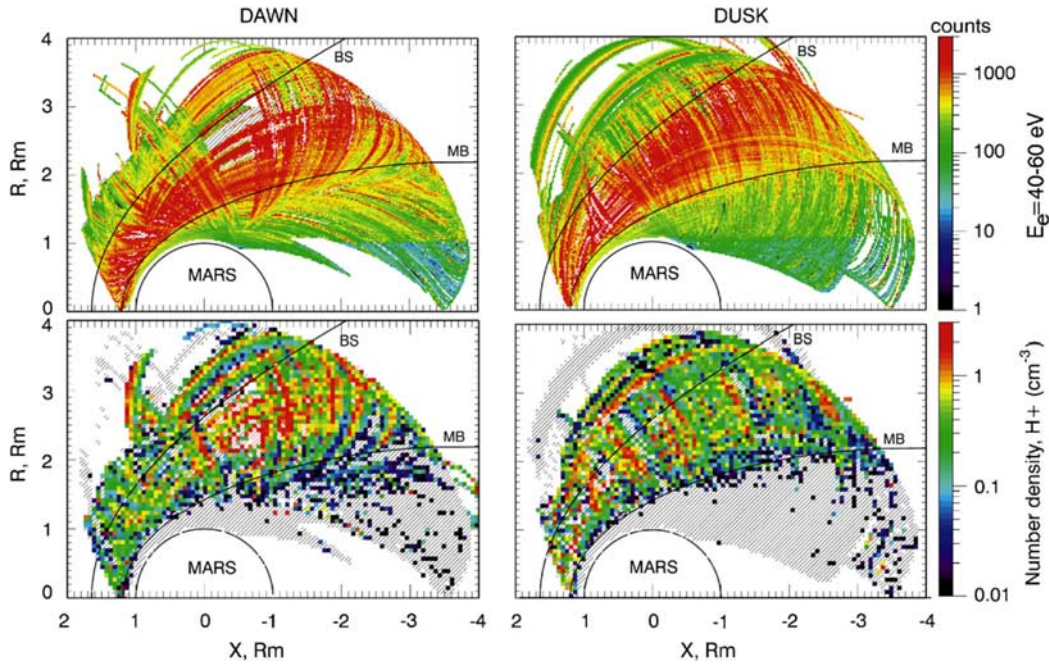
[1]Physikalisches Institut, University of Bern, Bern, Switzerland.
[2]Finnish Meteorological Institute, Helsinki, Finland.
[3]Swedish Institute of Space Physics, Kiruna, Sweden.
[4]Geospace Physics Laboratory, NASA Goddard Space Flight Center, Greenbelt, Maryland, USA.
[5]Department of Physics, West Virginia University, Morgantown, West Virginia, USA.

Figure 1. Maps of the median values of the electron fluxes (with energies $E_e = 40–60$ eV) and the proton number density at the dawn and dusk sides in MSO cylindrical coordinates with a grid size of 0.1 R_M. Measurements are from the ELS and IMA sensors, respectively, for the period from 1 February 2004 and 1 February 2006. Solid curves show the position of the bow shock, BS, and induced magnetospheric boundary, MB. Figure 1 reprinted from *Dubinin et al.* [2008], copyright 2008, with permission from Elsevier.

way through a pure hydrogen atomic gas with a density $n_H(r)$ the ENA production equation reads:

$$J_{ENA} = \sigma \int_{LOS} dr \, n_H(r) j_p(r), \qquad (1)$$

with J_{ENA} the ENA intensity in cm^{-2} sr^{-1} s^{-1} and σ the charge exchange cross-section. For 1 keV, which is the typical energy of ENAs measured with NPD, $\sigma \approx 2 \cdot 10^{-15}$ cm^2 for a proton-hydrogen reaction, and $\sigma \approx 1 \cdot 10^{-15}$ cm^2 for O$^+$-hydrogen charge exchange [*Lindsay and Stebbings*, 2005]. ENA measurements therefore reflect the plasma distribution as well as the neutral densities along the line-of-sight (LOS) of the sensor.

[7] Before Mars Express arrived at Mars, three different ENA sources were expected around a nonmagnetized planet with an atmosphere. NPD observations of the dayside of Mars confirmed the existence of an ENA albedo caused by solar wind ENAs that are scattered back from the dayside atmosphere [*Futaana et al.*, 2006a]. The NPD measurements also revealed a narrow ENA stream of shocked solar wind right above the sub-solar point in the magnetosheath [*Futaana et al.*, 2006b, 2006c; *Grigoriev et al.*, 2006; *Mura et al.*, 2007]. At the nightside of Mars, the expected flow of tailward (moving towards the magnetotail) ENAs was also detected [*Galli et al.*, 2006b]. Unperturbed solar wind protons, magnetosheath plasma, and accelerated planetary ions are possible parent ions for this tailward ENA flow, the latter parent population being the only one that also may produce a measurable amount of oxygen ENAs. Exospheric

hydrogen is the most important neutralizing agent because of its large scale height as we will show below.

[8] A first study on the tailward flowing ENAs was presented by *Galli et al.* [2006b]. The present work is a comprehensive re-evaluation of the earlier study, which became necessary because the final calibration of the NPD sensor became available since the publication of the earlier study [*Grigoriev*, 2007]. Moreover, we added data from all NPD sensor modes to the present analysis. Finally, we performed a statistical comparison of the observations with ENA model predictions. A similar study of the Venusian nightside ENAs, based on data obtained with the ASPERA-4/NPD sensor on Venus Express, has been presented recently by *Galli et al.* [2008].

[9] We will briefly describe the NPD sensor in section 2, before presenting the database that underlies this work (section 3). In section 4 we will show the global intensity images of tailward flowing hydrogen ENAs; they will be compared to model predictions in section 5. Also, a brief comparison to the H-ENA tailward flow measured with ASPERA-4/NPD at the nightside of Venus is given. The search for oxygen ENAs will be summarized in section 6, followed by the discussion in section 7.

2. NPD Sensor

[10] NPD is designed to measure hydrogen and oxygen ENAs at energies between 0.2 and 10 keV, using the time-of-flight (TOF) technique. Angular resolution is provided by having two NPD sensors (NPD1 and NPD2), each with three angular channels (NPD1_0, NPD1_1, NPD1_2,
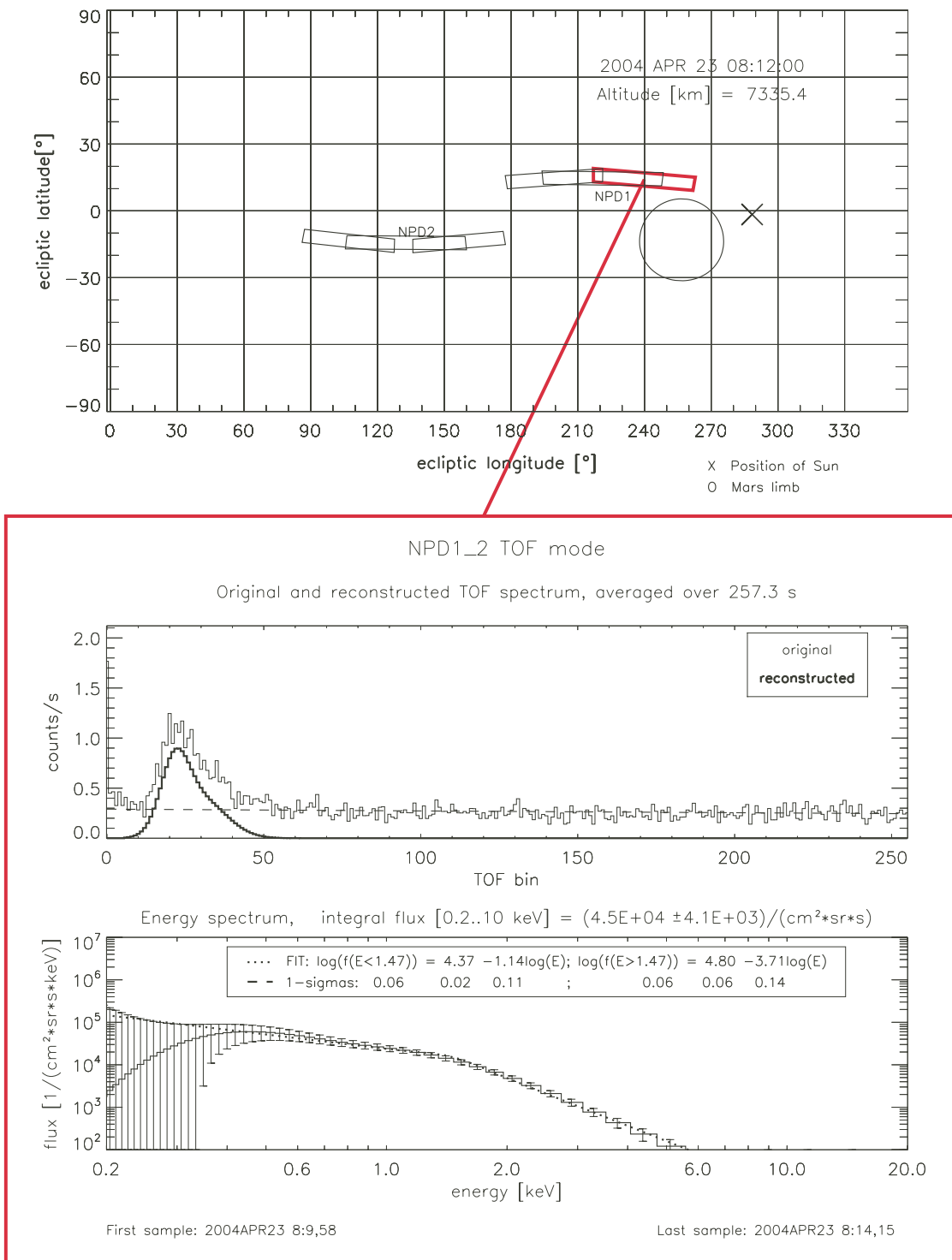
Figure 2. (top) Location of the six field-of-views of NPD is shown in the ecliptic coordinate system. Also the Mars limb (solid line) and the location of the Sun (cross) are indicated. (middle) Typical H-ENA TOF spectrum (thin line) from inside the IMB at the nightside of Mars on 23 April 2004 recorded with channel 2 of NPD1 (NPD1_2). The thick line is the reconstructed ENA signal with the background removed. (bottom) Energy spectrum calculated from the TOF spectrum.

NPD2_0, NPD2_1, and NPD2_2). Each NPD channel has a field-of-view (FOV) of 40° × 6° (see Figure 2, top, for the viewing directions) giving a total instantaneous FOV of 180° × 6° [*Barabash et al.*, 2006; *Grigoriev*, 2007]. We can distinguish between hydrogen and oxygen ENAs mainly because their TOF values do not overlap for most energies that occur in the Martian plasma environment.

[11] NPD can be run in three different data acquisition modes. BINNING mode offers high temporal resolution (see Figure 3, bottom) with a resolution of only 16 TOF
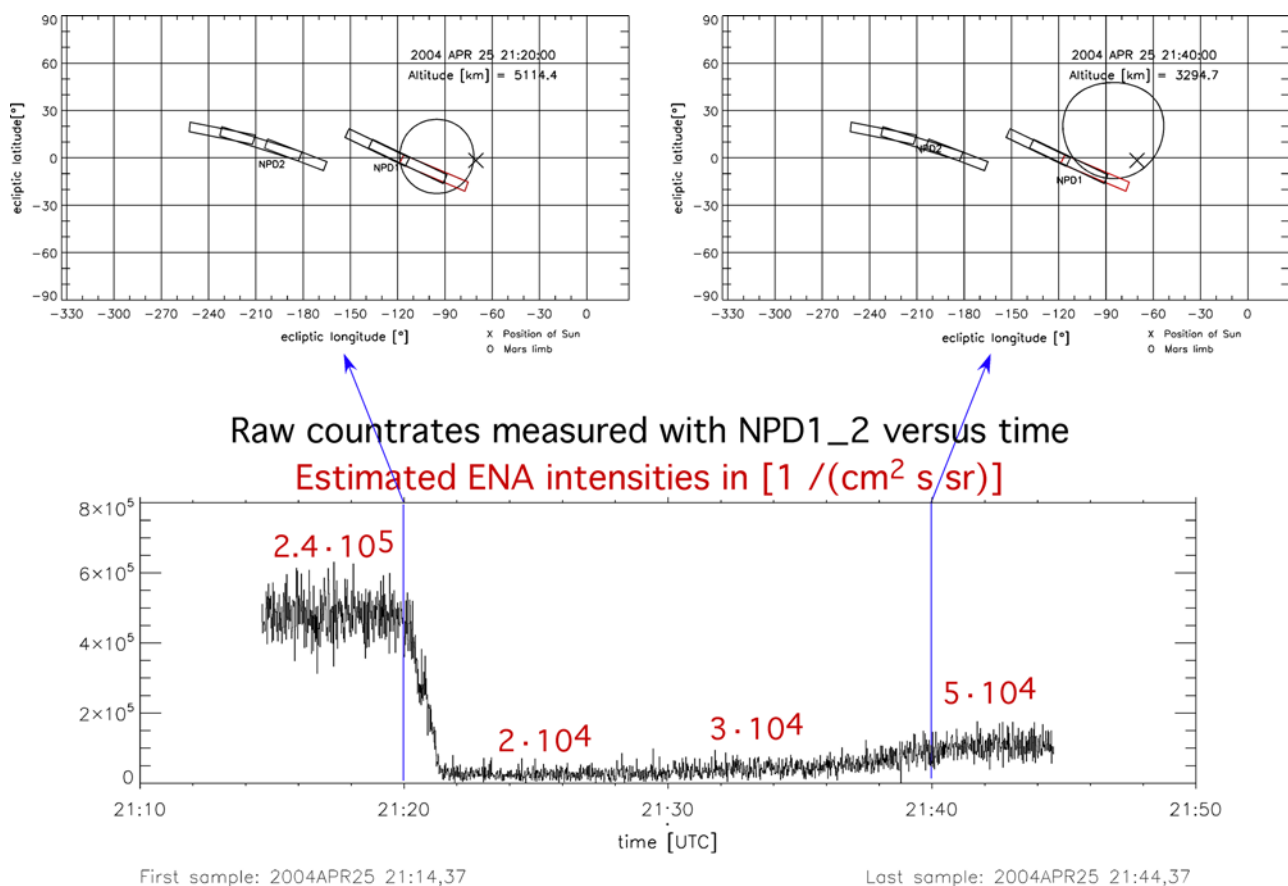
Figure 3. (top) Two observation configurations for 21:20 UT, when Mars Express was about to enter the shadow of Mars, and for 21:40 UT, when the eclipse period approached the end. (bottom) Intensity of tailward flowing H-ENAs as a function of time, seen in channel NPD1_2 on 25 April 2004, 21:14−21:45 UT. The black line shows the raw count rates (including background) with 1-s resolution; the red numbers are integral ENA intensities derived from a few minutes integration time.

bins. RAW mode and TOF mode offer 256 TOF bins between 0 and 2048 ns (see Figure 2, middle) but feature a low duty cycle and therefore have a lower temporal resolution. In this work we have included measurements obtained with all three data acquisition modes. We will focus on the integral intensity of ENAs because this is the parameter that is most reliably derived from all different data acquisition modes.

[12] Apart from ENAs, NPD is also sensitive to UV photons. Observations with the Sun in the FOV therefore have to be avoided. Figure 3 shows the closest possible approach of the FOV to the Sun outside the Mars shadow. On the other hand, the UV sensitivity of NPD can also be used to estimate the neutral hydrogen exospheric density with the Lyman-α radiation as a proxy [*Galli et al.*, 2006c].

3. Database

[13] For this study we included all NPD measurements during which the spacecraft was inside the IMB at the nightside of Mars. Most of these observations fall into the period between 23 April and 26 May 2004. To estimate the extension of the IMB we relied on simultaneous ion and electron measurements with IMA and ELS. NPD measurements with poor counting statistics were excluded from

further analysis. The measurements were then divided into intervals of 1 to 10 min integration time, 1 min being enough only for the most intense ENA signals. All derived ENA intensities apply to the energy range from 0.2 to 10 keV. The detection threshold is $5 \cdot 10^3$ cm^{-2} sr^{-1} s^{-1}. The typical uncertainty (the combination of statistical and instrumental uncertainty) of intensities for a single time interval amounts to 20%.

[14] The reconstruction of differential ENA intensities from raw count rates follows the method established by *Galli et al.* [2006a]. As improvement over the first report on tailward ENAs [*Galli et al.*, 2006b] we have now completed the database for observations inside the IMB and we have incorporated the final laboratory calibration data for NPD [*Grigoriev*, 2007]. Compared to the estimates used in our first publication [*Galli et al.*, 2006b] the geometric factor has not changed but the detection efficiency is a factor of two higher. All ENA intensities therefore decrease by a factor of two.

[15] The time span covered by the NPD observations at the nightside of Mars corresponds to low solar activity (solar activity index is around 40, $F_{10.7}$ is around 100). Unfortunately, we do not know the exact angle of the interplanetary magnetic field B_{IMF} for a particular orbit, lacking a magnetometer on board Mars Express. This makes
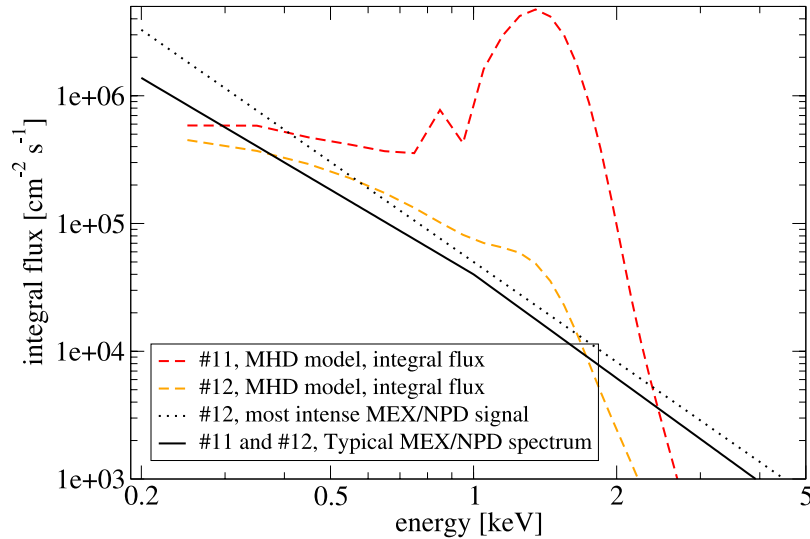
Figure 4. MHD model prediction for the energy spectrum of the integral ENA flux for spacecraft position 11 (red line) and 12 (orange line) versus typical energy spectra measured with NPD (black lines).

it harder to interpret the ENA tailward flow because planetary ENAs are expected to be organized around the B_{IMF} draping direction [*Lichtenegger et al.*, 2002]. About the solar wind parameters for particular orbits we do not know much either: IMA was not designed as a solar wind monitor, and there are several NPD observations for whose orbits no plasma measurements outside the bow shock exist at all. *Fränz et al.* [2006] find, as an average from February 2004 to February 2006, 300 to 400 km s^{-1} as best estimate for the median solar wind bulk speed and 1 to 3 cm^{-3} for the density of the unperturbed solar wind. This is a typical solar wind strength expected for 1.5 AU heliocentric distance.

4. Results

[16] Figure 2, top, shows the viewing directions of the 2×3 and FOVs of the NPD1 and NPD2 angular channels relative to the Mars limb (circle) and the Sun (cross) for a typical observation of tailward ENAs. Figure 2, middle, shows a typical example of raw TOF data of the tailward flowing hydrogen ENAs. The spectrum was measured with NPD1_2 channel with the viewing geometry given in panel 1 and accumulated over 4 min, where the original signal (thin line) and the reconstructed ENA signal (bold line) are indicated. In addition, the flat background from UV photons is indicated by the dashed line. The integral ENA intensities for the ENA tailward flow are in the range between 10^4 and 10^5 cm^{-2} sr^{-1} s^{-1}, and the intensity for the particular measurement presented in Figure 2 is $4.5 \cdot 10^4$ cm^{-2} sr^{-1} s^{-1}. The bottom panel in Figure 2 shows the ENA energy spectrum derived from the reconstructed TOF signal (bold line in middle panel), with 1σ-error bars and an estimate of the integral intensity. The derivation of the ENA energy spectrums works for energies between 0.3 keV and 5 keV, below and above this energy range the spectral values are obviously ill constrained by NPD measurement. The solid line gives a fit with a two-component power law energy spectrum with a roll-over around 1 keV. The NPD2 sectors that are directed toward the anti-Mars hemisphere, i.e., the

hemisphere when looking in zenith direction (see Figure 2, top) detect only a weak TOF signal corresponding to ENA intensities below $1 \cdot 10^4$ cm^{-2} sr^{-1} s^{-1}.

[17] Figure 3 shows an ideal spacecraft orientation and location to measure intense ENA signals: With up to $2.4 \cdot 10^5$ cm^{-2} sr^{-1} s^{-1} the signal measured on 25 April 2004, during $21:14-21:44$ UT, is the highest ENA intensity ever registered in the tailward flow at Mars. After 21:20 UT, the Sun disappears behind the planetary limb and the ENA signal drops to $2 \cdot 10^4$ cm^{-2} sr^{-1} s^{-1} within 1 min. Unfortunately, it is not possible to reconstruct ENA intensities for significantly shorter time intervals because of the counting statistics. After Mars Express has entered into eclipse, NPD1_2 continues to measure a weak ENA signal because the FOV is directed close to the limb and a part of the ENAs originating from the hot solar wind in the magnetosheath are emitted into the shadow of Mars.

[18] The intensity variation over minutes exhibited in Figure 3 are clearly spatial effects as the spacecraft position changes relative to the Mars and Sun direction. There are also temporal oscillations but among a dozen different time series no preferred oscillation period is found. This is different from the subsolar ENA jet at the dayside, which was found to oscillate with oscillation periods of 50 and 300 s [*Grigoriev et al.*, 2006]. For the nightside observations there are not enough data to conduct detailed investigations of temporal fluctuations, and we always face the problem of a large FOV size of at least $40° \times 6°$ and of a fast moving spacecraft. Moreover, we usually do not have simultaneous information of the unperturbed solar wind in front of the Martian bow shock or the B_{IMF} directions, which is a severe deficiency when discussing individual ENA observations.

[19] ENA signals that are strong enough can be inverted into energy spectra [*Galli et al.*, 2006a], which can be described by a two-component power-law (see Figure 2 for a typical example). Considering all of these energy spectra we find a median roll-over around 1.0 keV, a median slope at lower energies of -2.2, and a slope of -2.7 at energies above 1.0 keV. These results are in agreement with our
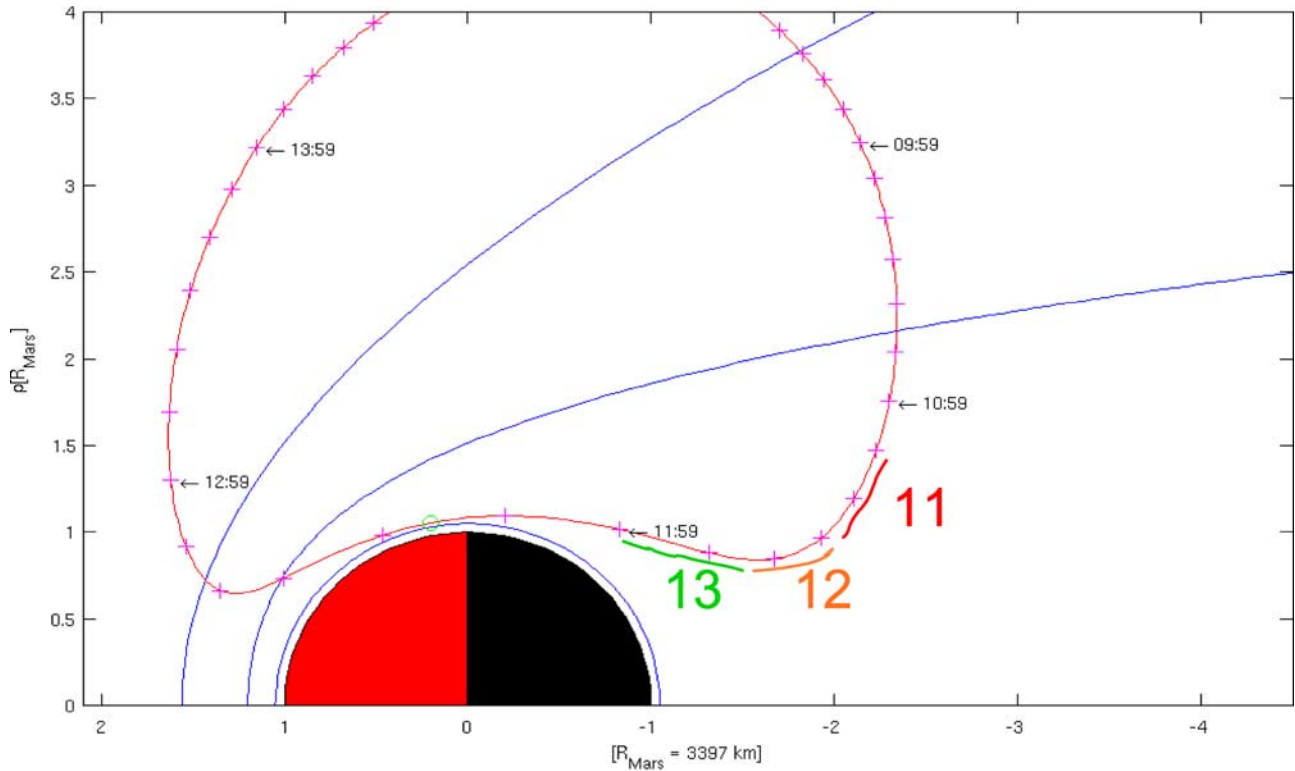
Figure 5. Orbit plot of Mars Express on 3 May 2004 in cylindrical coordinates. The time periods during which the ENA measurements incorporated in images 11, 12, and 13 were obtained are marked with colored lines.

previous report [*Galli et al.*, 2006b]. These energy spectra are consistent with ENAs from shocked solar wind.

[20] Figure 4 shows the comparison of the MHD model prediction and the NPD measurement where two model ENA energy spectra are given: one ENA spectrum for unperturbed solar wind ions if the Sun is outside the Mars limb (red line), and one spectrum for a spacecraft position inside the Mars eclipse (orange line). The total flux rate is lower for the MHD ENA spectrum inside the Mars eclipse, and the spectral shape is smeared to a two-component power law with a roll-over at 1.5 keV (the spacecraft positions 11 and 12 correspond to the vantage points in Figures 6 and 7). The smeared energy spectrum is similar to the energy spectra actually observed with NPD, the solid and dashed black lines shown in Figure 4. The ENA spectrum for unperturbed solar wind ions is considerably different from the observed spectra. However, we do not have a NPD measurement from the solar direction (see image shown in Figure 6) because NPD cannot observed with the Sun inside the FOV. Actually, there are very few well-constrained energy spectra from the near-Sun direction. Therefore, we cannot confirm that the transition in the ENA spectra is as pronounced as suggested by the MHD model. Note that the height of the observed spectrum is arbitrary in Figure 4 since NPD did not cover the maximum of the ENA outflow for image 11 (Figure 6).

[21] For the quantitative comparison with ENA models we will now focus on the global image of integral intensities. From single measurements such as those shown in Figure 3 we synthesized 3 ENA intensity images that contain virtually (714 out of 792) all measurement intervals. The measurement intervals were organized in three different plot categories (11, 12, and 13) for which the Mars center varies within ±10° at most and the variations in altitude correspond to a variation of apparent planetary radius of ≤ 10°. The vantage point of the spacecraft for the three categories is depicted in Figure 5. To create composite images the single intensity measurements were averaged over a 10° × 10° square mesh. The results are shown in Figures 6, 7, and 8. These three images update and complete Figure 9 in the report of *Galli et al.* [2006b]. The plots are shown in a cylindrical projection of the Mars Solar Orbital (MSO) reference frame, the x-axis is the MSO longitude, the y-axis is the MSO latitude in degrees. The MSO reference frame is defined as follows: X points from Mars to the Sun, Z points to the North pole of the Martian orbital plane. By this definition, the Sun direction is always at (0°/0°). Bins that are covered more than once by the NPD FOV are shown in color corresponding to the observed ENA intensity. The identical color scale is used for all images in this work. Pixels that have not been covered are left white. Because of the fast spacecraft proper motion during the pericenter passage of Mars Express single measurements are associated with a FOV footprint of typically 50° × 10°. This has to be taken into account when comparing model images with a much higher angular resolution to the observations.

[22] The composite ENA images show the following big picture: Around the Mars limb close to the Sun direction (1 to 2) · 10⁵ cm⁻² sr⁻¹ s⁻¹ H-ENAs are seen. If the Sun is
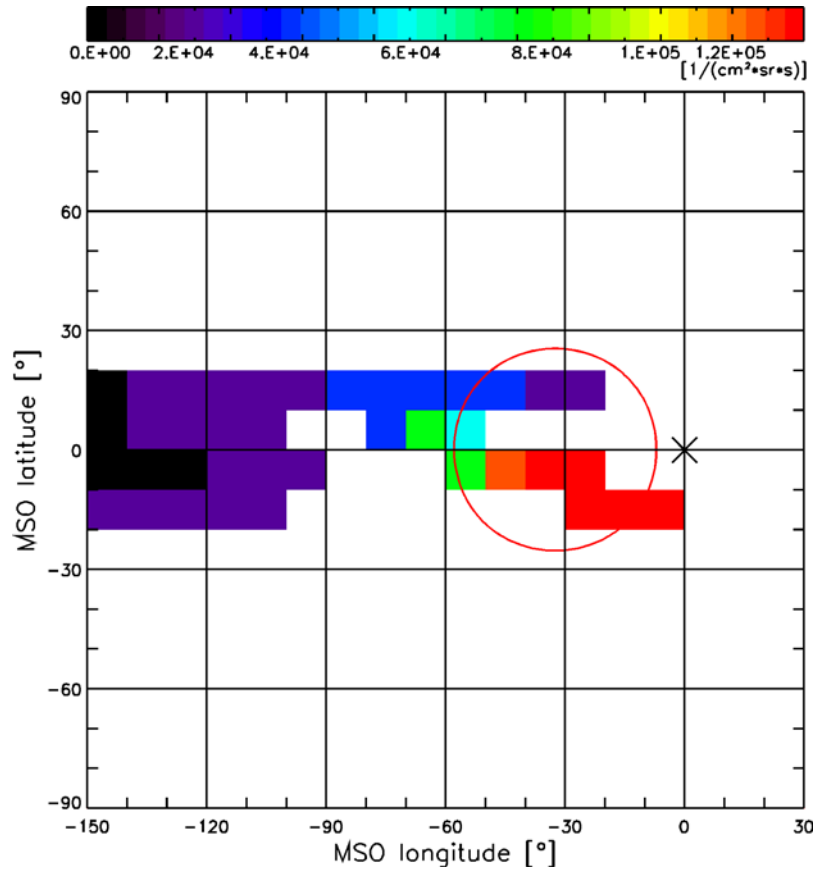
Figure 6. ENA intensity image of Mars 11, including 281 intervals from 23 April to 23 May 2004. The average FOV footprint is $40°F \times 6°$, the average solar zenith angle (SZA) of the spacecraft is $147°$, and the average altitude is $1.3 \, R_M$.

outside the limb and the NPD FOV is directed almost towards it this signal may reach up to $(2.4 \pm 0.8) \cdot 10^5 \, \text{cm}^{-2} \, \text{sr}^{-1} \, \text{s}^{-1}$. The ENA intensities decrease as the FOV is directed to the limb further away from the Sun direction, but distinct signals of up to $4 \cdot 10^4 \, \text{cm}^{-2} \, \text{sr}^{-1} \, \text{s}^{-1}$ are still seen (blue pixels in Figures 7 and 8). These signals cannot be explained as a spatial smearing effect of the FOV size, they originate really from the exosphere around the far-Sun limb. The nightside of the planet itself and the deep space, on the other hand, do not emit ENA signals above an intensity of $1 \cdot 10^4 \, \text{cm}^{-2} \, \text{sr}^{-1} \, \text{s}^{-1}$ (see the black areas in Figures 7 and 8). The boundary between the purple and black area (around $-100°$ longitude in Figure 8) marks the end of the region of detectable ENA production. The exact transition is a little arbitrary because the size of the NPD FOV broadens the apparent ENA outflow considerably. Nonetheless, Mars is a broad ENA source. In all three ENA images the entire Sun-ward hemisphere emits ENAs, except the Mars surface itself.

[23] The intensity of the maximum ENA outflow and its concentration around the limb close to the Sun direction are consistent with H-ENAs from shocked solar wind but as we will show in the next section 5 the opening angle of the outflow (up to $60°$ around the Sun direction) is hard to reconcile with a model of pure shocked solar wind ENAs. The opening angle of the ENA tailward flow, α, as observed in the ENA images (Figures 6–8) should scale with the plasma temperature of the parent ions around the terminator with:

$$\alpha \approx \arctan \sqrt{k_B T / E} \qquad (2)$$

where k_B is the Boltzmann constant, T is the ion temperature, and E is energy corresponding to the bulk flow of the plasma. If the tailward ENA flow is produced only from shocked solar wind, i.e., magnetosheath ions, equation (2) implies for $\alpha = 60°$ a temperature of the plasma between bow shock and IMB of $k_B T = 0.5$ keV, assuming a flow velocity of 200 km s^{-1} [*Fränz et al.*, 2006]. This plasma temperature is higher than the 0.15 keV established by *Fränz et al.* [2006] from proton measurements in the magnetosheath. This discrepancy is statistically significant, as will be elaborated in section 5. The thermal energy of the unperturbed solar wind is even two orders of magnitude smaller than its kinetic energy, which implies a scatter angle α of a few degrees (from equation (2)). Therefore, the contribution of unperturbed solar wind ENAs can safely be neglected as soon as the spacecraft is inside the Mars shadow (Figures 7 and 8).

[24] The black and purple pixels of the nightside itself indicate an upper limit of nightside ENA emission of $1 \cdot 10^4 \, \text{cm}^{-2} \, \text{sr}^{-1} \, \text{s}^{-1}$. Such an emission would be produced by protons that precipitate into the atmosphere on the nightside of the planet where they are neutralized and
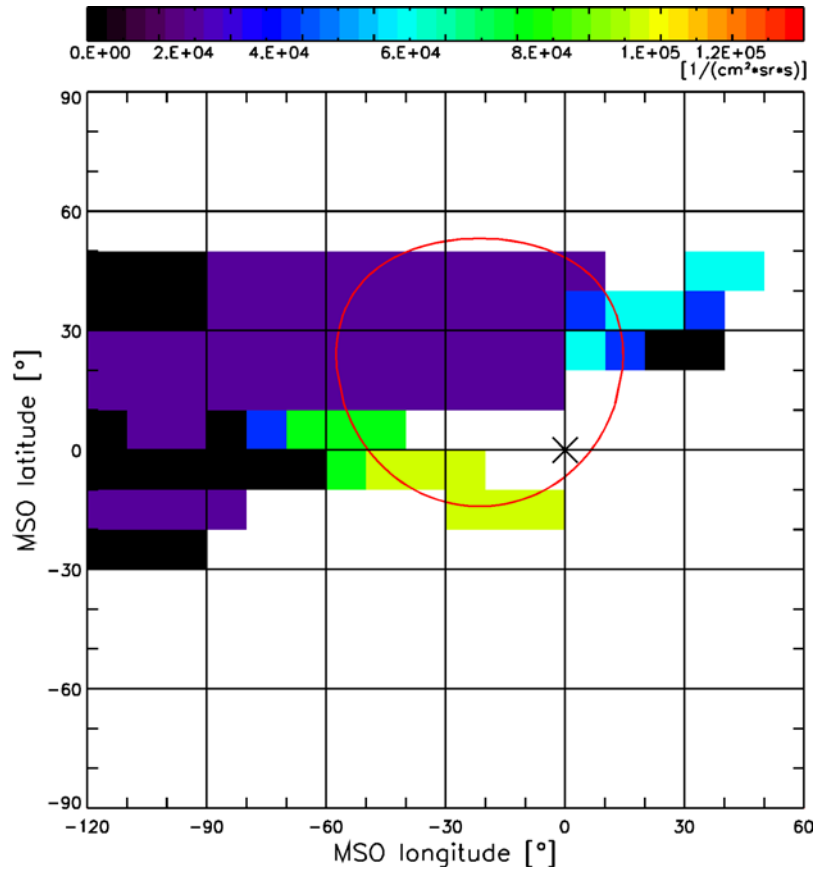
Figure 7. ENA intensity image of Mars 12, including 249 intervals from 23 April to 23 May 2004. The average FOV footprint is $50° \times 10°$, the average SZA is $152°$, and the average altitude is $0.8 \, R_{\mathrm{M}}$. Color scheme is the same as in Figure 6.

partially scattered back. This process has been observed with NPD above the dayside of Mars [*Futaana et al.*, 2006a]. Assuming a backscatter efficiency of 58% for the neutralized ions [*Kallio and Janhunen*, 2001] the NPD images impose an upper limit on protons that flow inside the magnetotail towards the nightside of Mars:

$$j_{\mathrm{H+}} < \frac{1}{0.58} 2\pi \times 10^4 \mathrm{cm}^{-2}\mathrm{sr}^{-1}\mathrm{s}^{-1} = 1 \cdot 10^5 \mathrm{cm}^{-2}\mathrm{s}^{-1}. \quad (3)$$

[25] The vast majority of the anti-Mars hemisphere was not covered or, where covered, it was found to emit less than $1 \cdot 10^4 \, \mathrm{cm}^{-2} \, \mathrm{sr}^{-1} \, \mathrm{s}^{-1}$ (black pixels in Figure 8). The single occasions when NPD detects a signal of $1 \cdot 10^4 \, \mathrm{cm}^{-2} \, \mathrm{sr}^{-1} \, \mathrm{s}^{-1}$ are still too close to the Martian limb to decide whether the weak ENA signals are due to anti-tailward flowing ENAs inside the IMB or whether they have a nonplanetary origin. The ENA intensity images shown in this work only impose an upper limit of a few $10^4 \, \mathrm{cm}^{-2} \, \mathrm{sr}^{-1} \, \mathrm{s}^{-1}$ on possible non-planetary H-ENAs. This question is discussed in detail elsewhere [*Galli et al.*, 2006a; *Wurz et al.*, 2008].

5. Statistical Comparison of the Observed H-ENA Tailward Flow With ENA Models

[26] To predict the ENA production of a planet, two components are required according to equation (1): a simulation of the plasma environment and a model of the neutral exosphere. For the plasma we have relied on the empirical model presented by *Kallio et al.* [1997] and on the MHD calculation of *Ma et al.* [2002]. Both models only include solar wind protons. To reproduce the three ENA images shown in Figures 6, 7, and 8 we have then evaluated equation (1) by combining the predicted proton flow with a neutral exosphere model. The latter is based on a Chamberlain model [*Chamberlain and Hunten*, 1987], the only input parameters required are the exobase density and temperature of the exospheric components. The ENA model predictions used in this work have been compared to each other by *Gunell et al.* [2006b]. We will now compare the models with the ENA measurements. This comparison will show whether the models also reproduce the global picture of solar wind interaction with the Martian atmosphere correctly by simulating by the global plasma distribution, and from that the ENA emission using a model of the exospheric gas densities. Since we can easily vary the exospheric parameters in the two models this comparison will also constrain some of the neutral exospheric densities. The ENA outflow is of course only one of several observational constraints for the models. The input parameters of the ENA model prediction must also be consistent with independent measurements of ion and neutral densities. Among all model parameters, the solar wind dynamic pressure and the density and temperature of the neutral
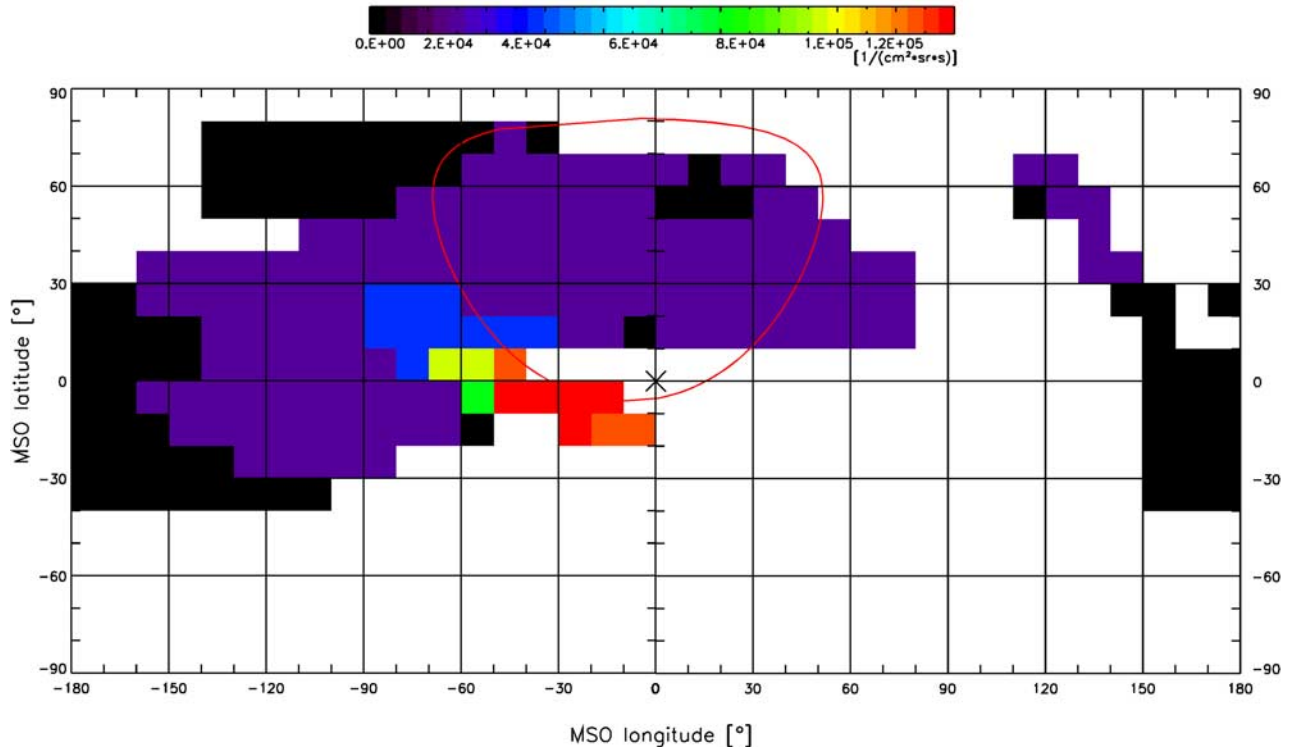
Figure 8. ENA all sky intensity image of Mars 13, including 184 intervals from 27 April to 26 May 2004. The average FOV footprint is $60° \times 20°$, the average SZA is $143°$, and the average altitude is $0.45\ R_M$. Color scheme is the same as in Figure 6.

hydrogen exosphere have the biggest effect on the predicted ENA outflow.

[27] For the solar wind parameters the empirical model assumes the following values: $n_{SW} = 2.5$ cm^{-3}, $T_{SW} = 15$ eV, and $v_{SW} = 400$ km s^{-1}. For the MHD model, *Ma et al.* [2002] assumed $n_{SW} = 4$ cm^{-3}, and $v_{SW} = 500$ km s^{-1}. The difference between the two models corresponds to the plausible range of uncertainty about the true solar wind plasma parameters in spring 2004. More extreme deviations from nominal solar wind conditions need not be studied since the ENA images shown in Figures 6, 7, and 8 are averages over one month of observations. Given the limited number of ENA observations available, we cannot investigate the effect of the orientation of the upstream B_{IMF} on the ENA emission, using IMF directions from MGS data as has been done in other studies [e.g., *Barabash et al.*, 2007a]. Regarding the effect of the crustal fields on the ion populations it has been concluded that they do not significantly affect the overall ion distribution, although the strongest anomalies have a small effect on the local ion outflow [*Nilsson et al.*, 2006]. Therefore, we do not consider the crustal field in our analysis.

[28] The exospheric densities show a much higher degree of uncertainty in the literature. As starting point we define a favorite scenario for the Martian neutral exosphere at low solar activity, for which the parameters are listed in Table 1. The neutral hydrogen is the most important exospheric species for the ENA production. In contrast, the hydrogen ENA observations are not sensitive to neutral helium (too tenuous and the cross-section is too small). Probably, H$_2$ does not affect the H-ENA production either, the

corresponding charge exchange cross-section is 5 times lower than for a H$^+$-H reaction. The hot oxygen component is also of minor importance because of the presence of hot hydrogen that dominates the ENA production at high altitudes. The cold hydrogen component is constrained by the UV limb emission measurements with NPD and SPICAM: for the year 2004 *Galli et al.* [2006c] find a very low value of a few 10^{10} m^{-3} for the North pole region, and for the year 2005 J. Y. Chaufray et al. (Lyman alpha detection of a hot hydrogen exospheric component by SPICAM on Mars Express, submitted to Icarus, 2008) derive $1 \cdot 10^{11}$ m^{-3} and $2 \cdot 10^{11}$ m^{-3} above the subsolar region and the terminator. The hot hydrogen component is found by both teams to be $1 \cdot 10^{10}$ m^{-3} at the exobase, with a temperature of $T > 500$ K. The parameters of the hot and thermal oxygen components are motivated by recent models of *Lichtenegger et al.* [2006] and *Chaufray et al.* [2007].

[29] The empirical plasma model, combined with the parameters listed in Table 1, yields ENA intensities that are similar to the NPD images within a factor of two for the regions of maximum ENA outflow. Figure 9 shows the model prediction calculated for the same planetary distance

Table 1. Default Model Parameters for the Martian Exosphere at Low Solar Activity

Species	Temperature (K)	Exobase Density (m^{-3})
Thermal H	200	$1 \cdot 10^{11}$
Hot H	600	$1 \cdot 10^{10}$
H$_2$	200	$1 \cdot 10^{12}$
Thermal O	200	$1 \cdot 10^{13}$
Hot O	4400	$4 \cdot 10^{9}$
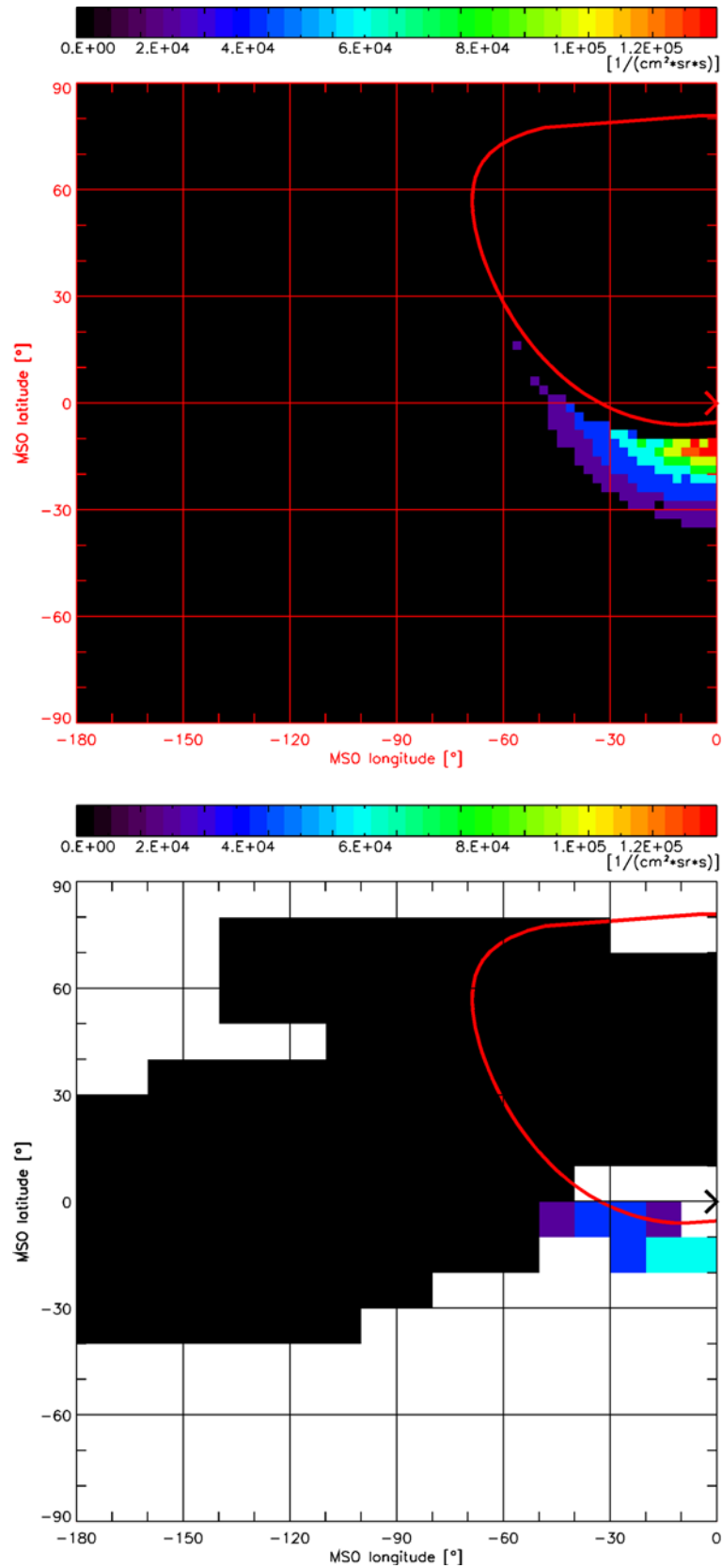
Figure 9. Predicted H-ENA outflow based on the empirical plasma model, calculated for the observation configuration of image 13 (Figure 8). (bottom) The smeared version of the (top) original model image.
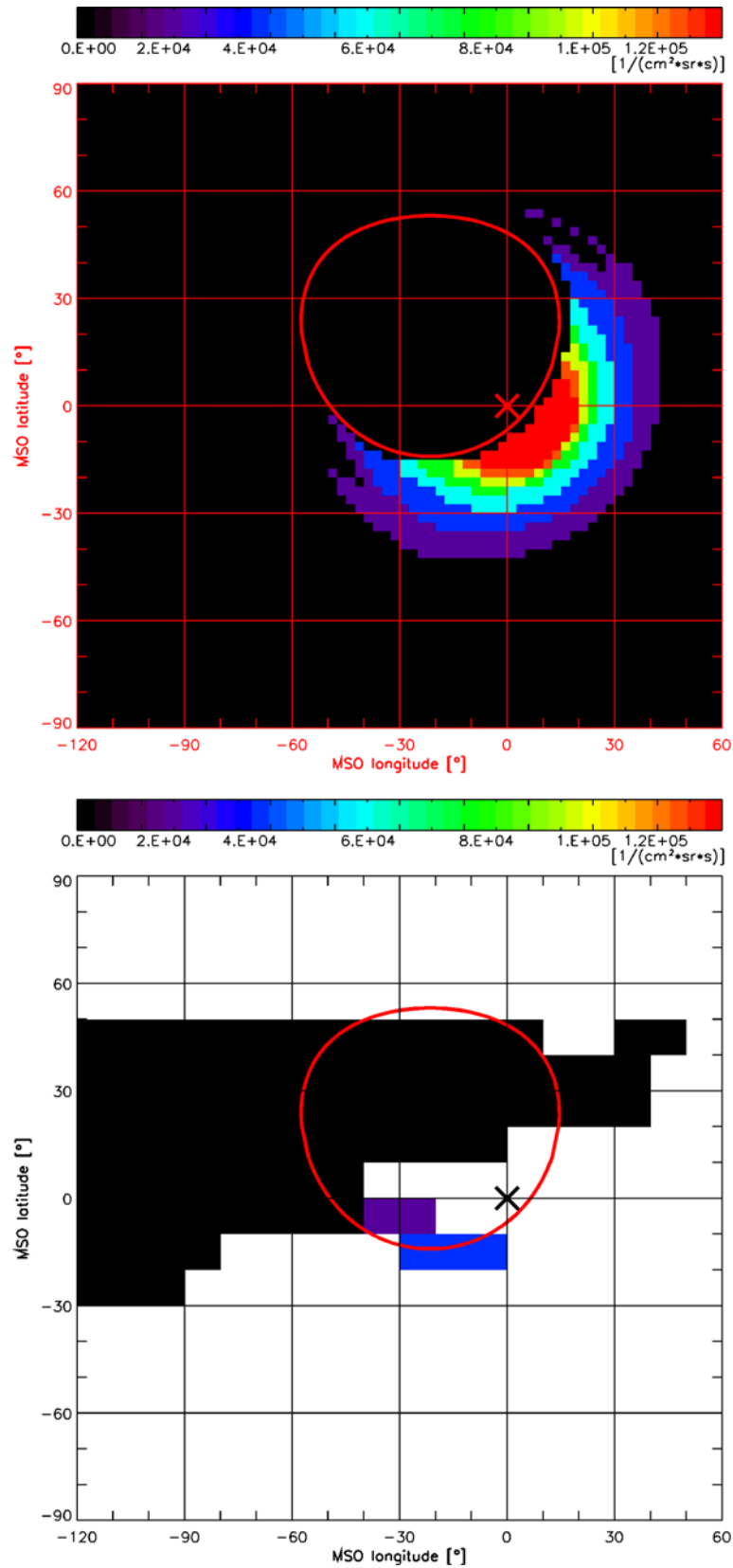
Figure 10. Predicted H-ENA outflow based on the MHD model, calculated for the observation configuration of image 12. (bottom) The smeared version of the (top) original model image. Color scheme is the same as in Figure 6.
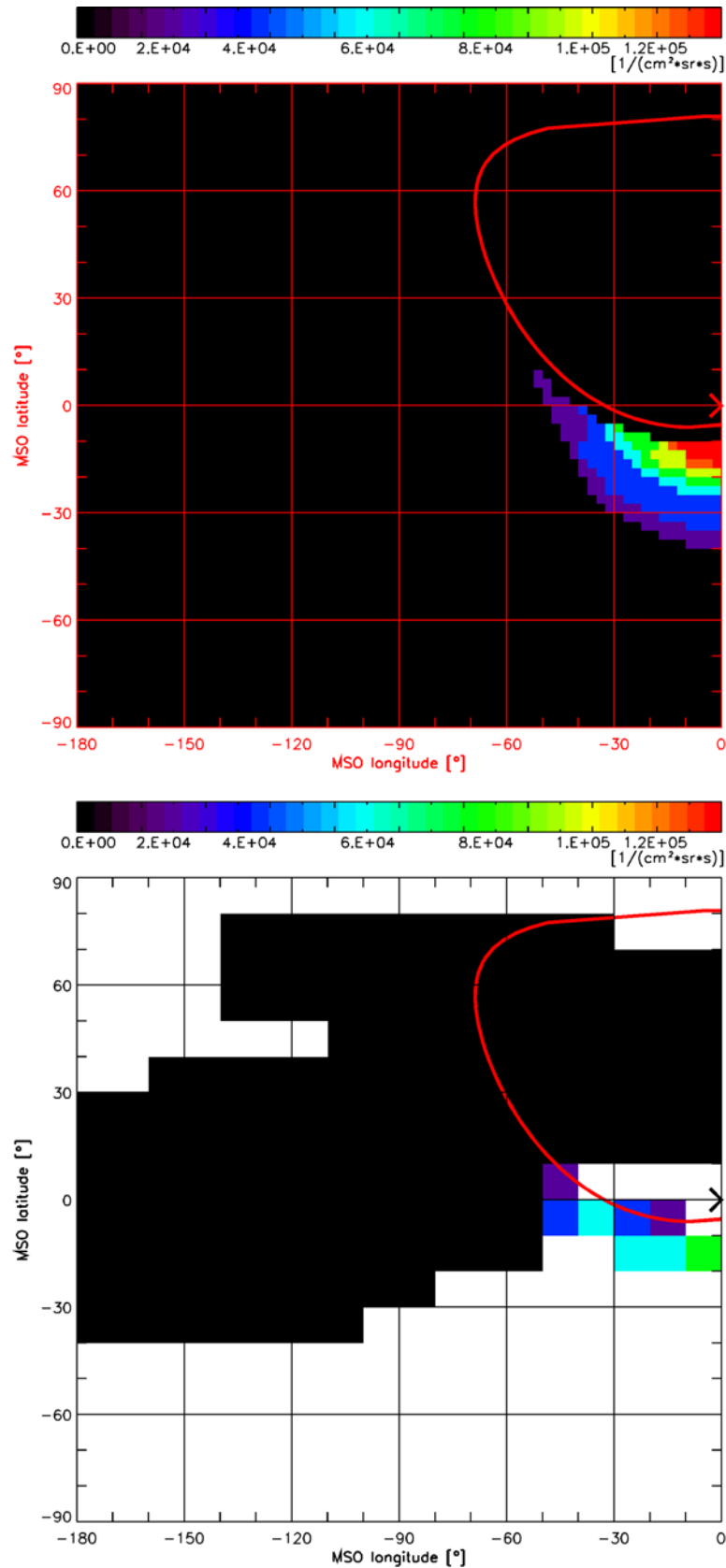
Figure 11. Predicted H-ENA outflow based on the MHD model, calculated for the observation configuration of image 13. (bottom) The smeared version of the (top) original model image. Color scheme is the same as in Figure 6.

and solar zenith angle as in Figure 8. The top panel shows the original model prediction with a grid size of $2.5° \times 2.5°$, and the bottom panel shows the same image, but convolved with the FOV footprints that are underlying the observation in Figure 8.

[30] The spatial distribution of the predicted outflow looks similar to the measurement, the maximum occurs close to the Mars limb symmetrical around the Sun position, while a faint halo of H-ENAs extends along the limb 90° away. Figure 9 is dominated by H-ENAs that result from charge exchange with neutral hydrogen. The H-ENAs neutralized with neutral oxygen form a thin ring-like structure but the H-ENAs originating from charge exchange with neutral hydrogen are more intense even for a LOS intersecting the exobase. Given the coarse spatial resolution of NPD, the H-ENA images are not sensitive to the exospheric oxygen, i.e., its density cannot be estimated from NPD observations.

[31] In spite of the similarity between Figures 9 and 8 there are two discrepancies between the empirical model and the NPD observations. First, the ENA intensities of the most intense pixels close to the Sun are predicted too low by a factor of two. Second, and statistically more significant, the observed outflow is much broader (ENAs are observed all along the Mars limb and from the exosphere outside the far-Sun limb) than predicted. This problem cannot be fixed by assuming a denser hydrogen exosphere.

[32] The resulting ENA images from the MHD model look identical to the ones obtained with the empirical model, the χ^2-fit probability (equation (4)) does not differ significantly. In Figures 10 and 11 we show the resulting images for two different MHD simulation runs, to be compared again to the NPD images 12 and 13 shown in Figures 7 and 8. Comparisons to image 11 are not shown because they do not add further information.

[33] To assess if the ENA model images (Figures 10 and 11, bottom) are a plausible fit to the NPD observations we calculate the square sum over all image pixels of observed ENA intensity j_{obs} minus predicted ENA intensity j_{mod}, divided by the uncertainty of the observed ENA intensity σ_j:

$$\chi^2 = \Sigma_i \left(\frac{j_{obs,i} - j_{mod,i}}{\sigma_{j,i}} \right)^2. \quad (4)$$

[34] Then we check the probability $P(\chi^2, f)$ that χ^2 from equation (4) is likely caused by chance or if the model prediction is really far from reality. The degree of freedom f is the number i of statistically reliable image pixels (approximately the number of independent measurement intervals) minus the number of model parameters. For the number of model parameters we set 12, appropriate to describe the solar wind plasma parameters and the exospheric densities of the thermal and hot hydrogen. The typical uncertainties of single pixels σ_j are half as large as j_{obs}.

[35] For images 11 and 12 the default MHD model with the exosphere parameters described in Table 1 yields a very low fit probability of $P(\chi^2, f) < 10^{-6}$. Obviously, the model lacks something to correctly reproduce the observed ENA images shown in Figures 6 and 7. For image 13 the agreement is better but far from satisfying ($P = 1\%$). Roughly the same fit probabilities emerge for the empirical

plasma model. We conclude that the ENA models of shocked solar wind resemble the observations but the observed ENA outflow is significantly broader than predicted.

[36] A copy of NPD is operating since 2006 as part of the ASPERA-4 experiment [*Barabash et al.*, 2007b] on Venus Express. Recently, we presented a study of the tailward ENA flow observed with the ASPERA-4/NPD sensor [*Galli et al.*, 2008]. The ENA tailward flow at Venus is similar to the one seen at the nightside of Mars. The only difference is that the ENA outflow at Venus is concentrated in a narrower angular range. The opening angle of the ENA tailward flow at Venus is only 30° compared to 60° at Mars, although the large FOV footprints tend to blur the features. Note that the reference frame and the color scale of the ENA intensities are identical to the Mars images. The reason for Venus being a narrower ENA source is the stronger gravitational pull of Venus, which results in lower exospheric scale heights above the exobase. This difference was predicted by ENA models prior to Venus Express [*Gunell et al.*, 2006b]. Unlike for Mars, for Venus the measured ENA image can be reproduced with a MHD code that only takes into account shocked solar wind ENAs. One example is shown in Figure 12, where the upper panel shows the NPD image and the lower panel shows the MHD model image (again smeared by the FOV footprints). Although a compilation of several weeks of ENA measurements is also needed for Venus ENA images, similar to the present Mars observations, we find good agreement with the MHD model results. Thus, the effect of a variable B_{IMF} direction on the ENA image must be lower than the present image resolution.

[37] We have investigated the following ideas to explain the discrepancy between models and observations at Mars:

[38] 1. Increasing the exospheric densities of H_2, helium, oxygen or any other heavy species does not explain the width of the H-ENA outflow because the corresponding scale heights are much smaller than the ones of hydrogen. The tenuous hot oxygen component does not influence the H-ENA images anywhere because of the hot hydrogen component. We have verified with the empirical model that leaving away the exospheric oxygen altogether does not significantly alter the predicted H-ENA image. The neutral oxygen contributes to the H-ENA production only in a thin ring of a few 100 km around the exobase. An exobase density of 10^{14} m^{-3} for the cool oxygen would explain some of the ENA emissions at the Mars limb far away from the Sun. However, *Chaufray et al.* [2007] have deduced O$^+$ and O-ENA loss rates (see section 6) that are consistent with the ASPERA-3 observations [*Barabash et al.*, 2007a], assuming an oxygen exobase density of only $n_O = 10^{13}$ m^{-3}.

[39] 2. The cool and the hot hydrogen exosphere cannot be much denser without contradicting Lyman-α measurements made in 2004 [*Galli et al.*, 2006c] and 2005 (Chaufray et al., submitted manuscript, 2008). The temperature of the Martian thermal exosphere has been shown to be 200 K by several in situ and aerobraking measurements [*Lichtenegger et al.*, 2006], and the vertical profile of the hot hydrogen component does not vary significantly for arbitrarily high temperatures above 600 K [*Galli et al.*, 2006c]. In the future we want to investigate whether the Chamberlain model for the density profile is an oversimplification, resulting in too low densities at high altitudes. But we doubt that this could explain the entire discrepancy. To see if the neutral hydrogen
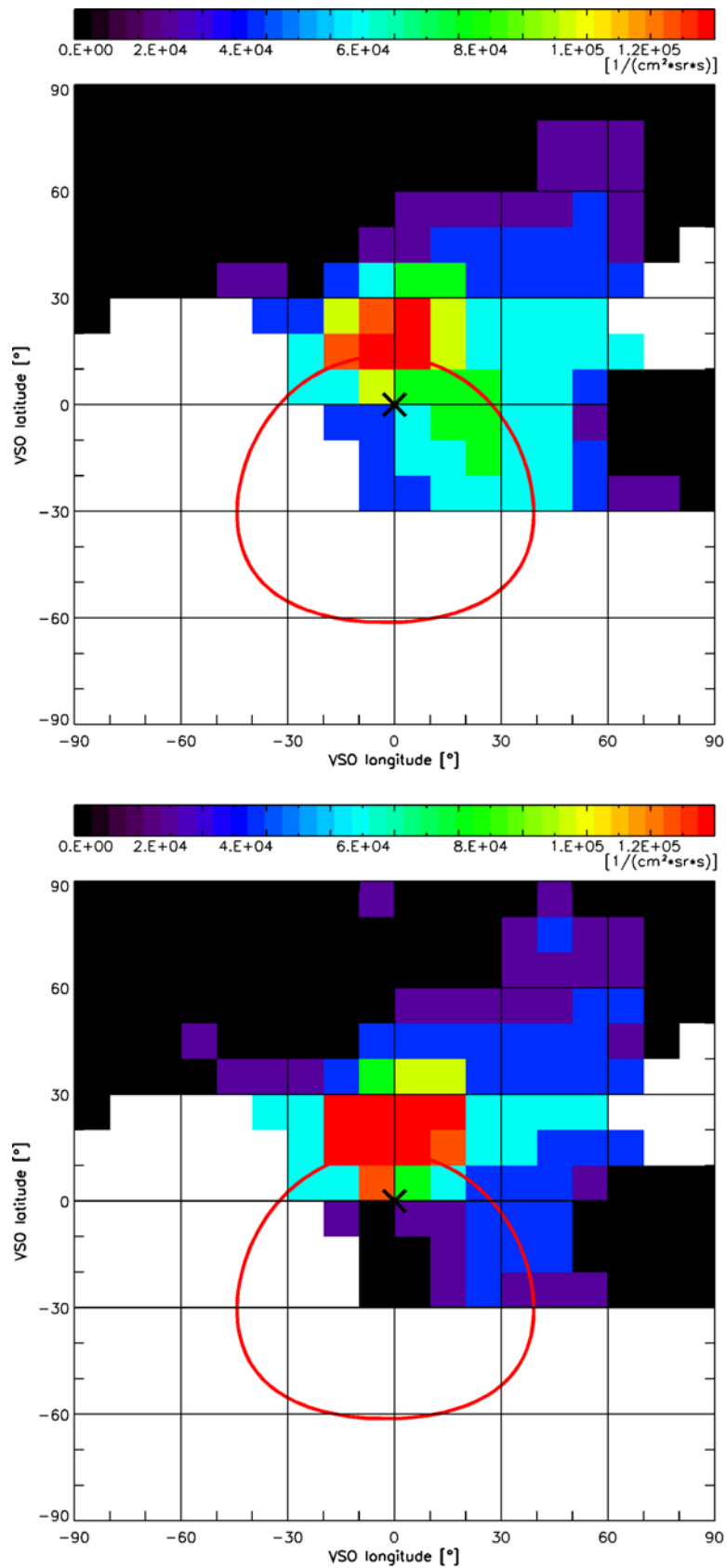
Figure 12. H-ENA image of the nightside of Venus, adapted from *Galli et al.* [2008]. (top) The ASPERA-4/NPD image obtained in August 2006. (bottom) The smeared version of the MHD model image for the same observation configuration. The format and the color scale are identical to the ENA images of Mars.

exosphere is responsible for the shortcomings of the model we have just varied the predicted ENA intensity by $c \times j_{ENA}$, with $c = 1$ to 10. This is equivalent to varying the exobase densities of the thermal hydrogen between 10^{11} and 10^{12} m^{-3} and the one of the hot component between 10^{10} and 10^{11} m^{-3}. The results are not satisfying. First, the optimized c, which minimizes χ^2 of equation (4), is not consistent for different images; for image 12 $c = 6$, and for image 13 $c = 2$. Second, even for optimized c the absolute fit probability P is still below 10^{-3} for images 11 and 12. Even with a hot hydrogen component whose exobase density is an order of magnitude higher than measured by *Galli et al.* [2006c] and by Chaufray et al. (submitted manuscript, 2008) the model images do not reproduce the outflow lobe shown in Figure 8 by the blue and purple pixels, or in Figure 7 by the green pixels. It seems that other trajectories of the magnetosheath plasma or new ion populations are required to explain the ENA outflow far away from the Sun direction.

[40] 3. Extreme solar wind conditions offer no plausible explanation: The MHD model does not fit significantly better to the observations although the assumed solar wind flux upstream of the bow shock $n_{SW} v_{SW}$ is twice as high as in the empirical model.

[41] 4. Maybe the plasma temperature in the magnetosheath is underestimated by the models or the MHD approximation is insufficient for the shocked solar wind around Mars. At present, we are working on a hybrid plasma model to test this possibility.

[42] 5. As observed with NPD [*Futaana et al.*, 2006a] the dayside of Mars emits several 10^5 cm^{-2} sr^{-1} s^{-1} hydrogen ENAs. A part of this signal is caused by reflected ENAs, the other part is caused by solar wind protons that precipitate into the atmosphere before being neutralized and scattered back to space as ENAs. For the precipitating protons, equation (3) yields a flux of a few 10^6 cm^{-2} s^{-1} at subsolar point. According to model calculations by *Kallio and Janhunen* [2001] the flux of precipitating protons at the terminator region still reaches 1% to 10% of this value. The precipitating solar wind protons thus might explain the ENA signals of a few 10^4 cm^{-2} s^{-1} originating directly from the Mars limb. For the broad ENA outflow outside the limb another process has to be responsible.

[43] 6. The broad ENA outflow of several 10^4 cm^{-2} sr^{-1} s^{-1} (blue lobe in Figure 8) far away from the Sun direction might be explained with planetary protons that are swept away by the convective electric field from the exosphere around the terminator region. If the models show that we have to include planetary H-ENAs the lack of accurate magnetometer data poses a severe problem. Since we do not know the B_{IMF} draping direction we cannot organize the ENA data along the convective electric field direction to check for a correlation. The energy spectrum of planetary H-ENAs is similar to solar wind ENAs because planetary pick-up ions and shocked solar wind protons share comparable energies [*Lichtenegger et al.*, 2002].

6. Upper Limit of Observed O-ENAs at Mars

[44] Observing oxygen ENAs at Mars would directly reveal an atmospheric erosion process. If there is an observable oxygen ENA signal it is truly planetary since

in the solar wind the oxygen abundance is 5000 times lower than hydrogen. The most likely location to identify Martian O-ENAs is the tailward flow close to the limb. According to the laboratory calibration already an O-ENA signal of more than $1 \cdot 10^4$ cm^{-2} sr^{-1} s^{-1} is visible even in the presence of UV background and a H-ENA peak if the energy lies above 0.5 keV.

[45] For O-ENAs in the tailward flow of Mars we find, after implementing the new O-ENA instrument response [*Grigoriev*, 2007] for all observations inside the IMB from February to June 2004 an upper limit of $5 \cdot 10^4$ cm^{-2} sr^{-1} s^{-1} for 0.4 to 3.5 keV energy. This is the same result we found with a smaller data sample before [*Galli et al.*, 2006b].

[46] Figure 13 shows the best candidate for a real O-ENA signal. The measurement was obtained in BINNING mode, where the TOF bins 10 to 15 correspond to a TOF range of 486 ns to 1900 ns. If the ENA is a hydrogen atom this TOF range corresponds to energies below 0.1 keV. Since NPD is insensitive to H-ENAs below 0.1 keV, any signal registered in the TOF bins 10 to 15 has to be caused by UV photons or by O-ENAs (the last of the 16 TOF bins in Figure 13 would correspond to O-ENA energies around 0.4 keV). UV light, however, is known – from calibrations in the laboratory and from stellar Lyman-α observations during cruise phase – to produce a flat background in the TOF spectrum (see the TOF response in Figure 2). Figure 13 shows a clear bulge in the TOF spectrum at O-ENA energies around 1 keV. But this is the only occasion where such a feature is statistically significant against the flat UV background (estimated here by the count rate in the very last TOF bin) by a 3-sigma confidence interval. The corresponding O-ENA intensity amounts to only $(3 \pm 2) \cdot 10^4$ cm^{-2} sr^{-1} s^{-1}.

[47] As shown by *Galli et al.* [2006b], oxygen ENA intensities of a few 10^4 cm^{-2} sr^{-1} s^{-1} impose an upper limit on the global production rate of O-ENAs of the order of 10^{22} s^{-1}.

7. Discussion

[48] The present plasma models, combined with the neutral hydrogen and oxygen exosphere as observed during Mars Express, reproduce the observed hydrogen ENA outflow at the nightside within a factor of two. The tailward ENA flow seems to consist mainly of shocked solar wind ENAs. The nonobservation of oxygen ENAs is consistent with recent exosphere models as well. However, the outflow of ENAs at the limb and the terminator region far away from the Sun direction is much broader than predicted by current plasma models. The ENA images are a challenge for future model efforts. At present, our conjecture is that planetary protons and ENA limb emission due to proton precipitation into the atmosphere have to be included.

[49] We have tested various hydrogen exobase densities, and our preferred value is $1 \cdot 10^{11}$ m^{-3} within a factor of two. As long as new ion populations have to be included in the models to reproduce the ENA images we cannot be more accurate about the neutral hydrogen densities. But we confirm the earlier findings [*Galli et al.*, 2006c; Chaufray et al., submitted manuscript, 2008] that the neutral hydrogen exosphere is significantly thinner at low solar activity than theoretically predicted [*Krasnopolsky*, 2002]. For oxygen we only can give upper limits, and the other chemical
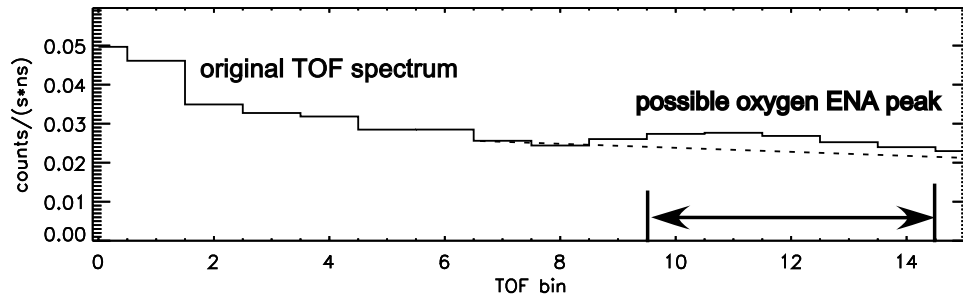
Figure 13. Original TOF spectrum measured with channel NPD2_0 on 18 May 2004, 22:18–22:22 UT at the nightside of Mars. This is the only NPD measurement with a significant TOF peak at O-ENA energies 0.4 to 3.5 keV (the five TOF bins marked with red). The bulge above the dashed line (estimate of the UV background) corresponds to an ENA intensity of $3 \cdot 10^4$ cm^{-2} sr^{-1} s^{-1}.

constituents of the Martian exosphere are not constrained by NPD measurements.

[50] For oxygen ENAs around Mars we find for all observations inside the IMB from February to June 2004 an upper limit of $5 \cdot 10^4$ cm^{-2} sr^{-1} s^{-1} in the energy range from 0.4 to 3.5 keV energy. This imposes on the global production rate of O-ENAs an upper limit of

$$Q_{\text{O-ENA}} = 10^{22} \text{ to } 10^{23} \text{s}^{-1} \tag{5}$$

[51] This value is consistent with the model prediction by *Chaufray et al.* [2007] who predict $Q_{\text{O-ENA}} = 4 \cdot 10^{22}$ s^{-1} of escaping O-ENAs for solar minimum condition. This gives us confidence that the recent oxygen exosphere models are approaching reality. Charge exchange reactions in general are not important for the atmospheric loss of oxygen at low solar activity [*Barabash et al.*, 2007a].

[52] We cannot compute integral fluxes (let alone total H-ENA production rates) directly from the NPD images because large areas, including the maximum outflow regions, were not covered with NPD. The global H-ENA production predicted by the default MHD model is $Q_{\text{H-ENA}} = 5 \cdot 10^{24}$ s^{-1}. This number is only 40% lower if the thermal hydrogen exospheric component is reduced by a factor of two and the oxygen density is reduced by an order of magnitude. This, once more, illustrates that exospheric oxygen is not important for H-ENA production. On the other hand, the true H-ENA production $P_{\text{H-ENA}}$ may be larger but does not exceed $1 \cdot 10^{25}$ s^{-1}. This upper limit is reached if a neutral hydrogen exobase density of $2 \cdot 10^{11}$ m^{-3} (Chaufray et al., submitted manuscript, 2008) is assumed for all solar zenith angles. The hydrogen ENA sources omitted from the MHD model do not contribute much to the total ENA production rate: The ENA albedo of the Martian dayside [*Futaana et al.*, 2006a] accounts for $Q_{\text{H-ENA}} = 1 \cdot 10^{24}$ s^{-1}. The tailward ENA flow far away from the Sun direction, which has been shown to be beyond the capabilities of the plasma models, is even more insignificant. Assuming $J_{\text{ENA}} = 5 \cdot 10^4$ cm^{-2} sr^{-1} s^{-1}, an aperture angle of 30° (equal to the IMB angle at the terminator) and a production region of roughly $A = \pi (R_M/2)^2$ we estimate for the additional tailward ENA flow a production rate of only:

$$Q = 2AJ_{\text{ENA}} \int_0^{2\pi} d\phi \int_0^{0.26} d\theta \sin\theta \cos\theta < 10^{22} \text{ s}^{-1} \tag{6}$$

At present, we therefore estimate the total hydrogen ENA production of Mars to be

$$Q_{\text{H-ENA}} = \left(6\,^{+4}_{-2}\right) \times 10^{24} \text{ s}^{-1} \tag{7}$$

The higher production rate derived by *Gunell et al.* [2005] resulted from assuming too dense exospheric hydrogen densities at Mars [*Krasnopolsky*, 2002]. For Venus, a recent comparison of the ASPERA-4/NPD measurements to a Venusian MHD model yields a total H-ENA production rate of $6 \cdot 10^{24}$ s^{-1} as well [*Galli et al.*, 2008]. We conclude that the total H-ENA production rates of Mars and Venus are similar for low solar activity.

[53] The loss rate of planetary hydrogen due to charge exchange reactions, $Q_{\text{H,CX}}$, has to be equal or smaller than equation (7) but the lower limit is difficult to derive from the NPD observations. Even if we can prove that planetary ENAs contribute to the NPD images, their contribution to the total loss is insignificant. Exospheric, i.e., planetary, hydrogen is ionised by charge exchange with a solar wind protons, and is picked up by the magnetosheath plasma flow and carried away from the planet to eventually become part of the solar wind. We try to constrain $Q_{\text{H,CX}}$ with NPD measurements nonetheless, because IMA is not able to estimate the loss rate of planetary H$^+$. Most of the hydrogen ENAs produced in the MHD model result from the charge exchange between solar wind protons and planetary hydrogen. The production rate of planetary H$^+$ thus is not much smaller than the $5 \cdot 10^{24}$ s^{-1} calculated from that model. All of these ions are produced outside the exobase, and the fraction that is produced outside the IMB will be picked up by the magnetosheath plasma and thus removed. This means that equation (7) is still the only quantitative estimate for the total hydrogen loss due to charge exchange. Taking all these uncertainties into account the ENA observations combined with the ENA model predictions suggest a total escape rate of planetary hydrogen, neutral and ionized, due to charge exchange reactions of the order of

$$Q_{\text{H,CX}} = 10^{24} \text{ s}^{-1} \tag{8}$$

The ASPERA-3 measurements show the following about the total loss rates of hydrogen and oxygen:

[54] The Mars exosphere is much thinner than previously modeled for low solar activity. Whereas the bulk, i.e., thermal, exosphere temperature is 200 K (and this varies only between 180 K and 230 K over solar cycle according to *Lichtenegger et al.* [2006]) there is a population of extremely hot hydrogen that is visible in the ENA tailward flow and that needs to be taken into account when discussing atmospheric erosion. We have also been able to estimate the total $Q_{H,CX}$; $Q_{O,CX} = 10^{23}$ s^{-1} has been measured with IMA [*Barabash et al.*, 2007a]. ASPERA-3 measurements have shown in general that charge exchange reactions are not important for the atmospheric erosion of hydrogen or oxygen at low solar activity. The situation may change for the oxygen loss at high solar activity [*Lundin et al.*, 1989]. Even so, the ASPERA-3 observations are all consistent with a global hydrogen loss of 10^{26} s^{-1} (dominated by Jeans escape) and a global loss of oxygen of 10^{25} s^{-1} (dominated by dissociative recombination) for any solar activity.

[55] ENA production on its own is not important as an atmospheric loss process but it allows for a quick, global overview on the interaction of the solar wind with planetary atmospheres. The ENA sensors flying on Mars Express and Venus Express allow us to perform quantitative research within a factor of two; the ENA images derived from NPD data will force theorists to refine the existing models of plasma and neutral exospheres of the nonmagnetized planets.

References

Barabash, S., et al. (2006), The analyzer of space plasmas and energetic atoms (ASPERA-3) for the Mars Express mission, *Space Sci. Rev.*, *126*, 113–164.

Barabash, S., A. Fedorov, R. Lundin, and J. A. Sauvaud (2007a), Martian atmospheric erosion rates, *Science*, *315*, 501.

Barabash, S., et al. (2007b), The analyzer of space plasmas and energetic atoms (ASPERA-4) for the Venus Express mission, *Planet. Space Sci.*, *55*, 1772–1792.

Bößwetter, A., T. Bagdonat, U. Motschmann, and K. Sauer (2004), Plasma boundaries at Mars: A 3-D simulation study, *Ann. Geophys.*, *22*, 4363.

Carlsson, E., et al. (2006), Mass composition of the escaping plasma at Mars, *Icarus*, *182*, 320.

Chamberlain, J. W., and D. M. Hunten (1987), *Theory of Planetary Atmospheres*, 2nd ed., Academic, Orlando, Fla.

Chaufray, J. Y., R. Modolo, F. Leblanc, G. Chanteur, R. E. Johnson, and J. G. Luhmann (2007), Mars solar wind interaction: Formation of the Martian corona and atmospheric loss to space, *J. Geophys. Res.*, *112*, E09009, doi:10.1029/2007JE002915.

Dubinin, E., M. Fränz, J. Woch, E. Roussos, S. Barabash, R. Lundin, J. D. Winningham, R. Frahm, and M. Acuña (2006), Plasma morphology at Mars, ASPERA-3 observations, *Space Sci. Rev.*, *126*, 209.

Dubinin, E., G. Chanteur, M. Fraenz, R. Modolo, J. Woch, E. Roussos, S. Barabash, R. Lundin, and J. D. Winningham (2008), Asymmetry of plasma fluxes at Mars. ASPERA-3 observations and hybrid simulations, *Planet. Space Sci.*, *56*, 832–835.

Fränz, M., E. Dubinin, E. Roussos, J. Woch, J. D. Winningham, R. Frahm, A. J. Coates, A. Fedorov, S. Barabash, and R. Lundin (2006), Plasma moments in the environment of Mars, *Space Sci. Rev.*, *126*, 165–207.

Futaana, Y., et al. (2006a), First ENA observations at Mars: ENA emissions from the Martian upper atmosphere, *Icarus*, *182*, 424.

Futaana, Y., et al. (2006b), First ENA observations at Mars: Subsolar ENA jet at Mars, *Icarus*, *182*, 413.

Futaana, Y., S. Barabash, A. Grigoriev, J. D. Winningham, R. Frahm, M. Yamauchi, and R. Lundin (2006c), Global response of Martian plasma environment to an interplanetary structure: from ENA and plasma observations at Mars, *Space Sci. Rev.*, *126*, 315.

Galli, A., et al. (2006a), Direct measurements of energetic neutral hydrogen in the interplanetary medium, *Astrophys. J.*, *644*, 1317.

Galli, A., P. Wurz, S. Barabash, A. Grigoriev, H. Gunell, R. Lundin, M. Holmström, and A. Fedorov (2006b), Energetic hydrogen and oxygen atoms observed on the nightside of Mars, *Space Sci. Rev.*, *126*, 267.

Galli, A., P. Wurz, H. Lammer, H. I. M. Lichtenegger, R. Lundin, S. Barabash, A. Grigoriev, M. Holmström, and H. Gunell (2006c), The hydrogen exospheric density profile measured with ASPERA-3/NPD, *Space Sci. Rev.*, *126*, 447.

Galli, A., M.-C. Fok, P. Wurz, S. Barabash, A. Grigoriev, Y. Futaana, M. Holmström, A. Ekenbäck, E. Kallio, and H. Gunell (2008), The tailward flow of energetic neutral atoms observed at Venus, *J. Geophys. Res.*, *113*, E00B15, doi:10.1029/2008JE003096.

Grigoriev, A. (2007), The neutral particle detector on the Mars and Venus Express missions, Ph.D. thesis, Inst. of Space Phys., Kiruna, Sweden.

Grigoriev, A., Y. Futaana, S. Barabash, and A. Fedorov (2006), Observations of the Martian subsolar ENA jet oscillations, *Space Sci. Rev.*, *126*, 299.

Gunell, H., M. Holmström, H. K. Biernat, and N. V. Erkaev (2005), Planetary ENA imaging: Venus and a comparison with Mars, *Planet. Space Sci.*, *53*, 433.

Gunell, H., et al. (2006a), First ENA observations at Mars: Charge exchange ENAs produced in the magnetosheath, *Icarus*, *182*(2), 431–438.

Gunell, H., M. Holmström, S. Barabash, E. Kallio, P. Janhunen, A. F. Nagy, and Y. Ma (2006b), Planetary ENA imaging: Effects of different interaction models for Mars, *Planet. Space Sci.*, *117*.

Kallio, E., and P. Janhunen (2001), Atmospheric effects of proton precipitation in the Martian atmosphere and its connection to the Mars-solar wind interaction, *J. Geophys. Res.*, *106*, 5617.

Kallio, E., J. G. Luhmann, and S. Barabash (1997), Charge exchange near Mars: the solar wind absorption and energetic neutral atom production, *J. Geophys. Res.*, *102*, 22,183.

Krasnopolsky, V. A. (2002), Mars' upper atmosphere and ionosphere at low, medium, and high solar activities: Implications for evolution of water, *J. Geophys. Res.*, *107*(E12), 5128, doi:10.1029/2001JE001809.

Lichtenegger, H. I. M., H. Lammer, and W. Stumptner (2002), Energetic neutral atoms at Mars: 3. Flux and energy distributions of planetary energetic H atoms, *J. Geophys. Res.*, *107*(A10), 1279, doi:10.1029/2001JA000322.

Lichtenegger, H. I. M., H. Lammer, Y. N. Kulikov, S. Kazeminejad, G. H. Molina-Cuberos, R. Rodrigo, B. Kazeminejad, and G. Kirchengast (2006), Effects of low energetic neutral atoms on Martian and Venusian dayside exospheric temperature estimations, *Space Sci. Rev.*, *126*, 469.

Lindsay, B. G., and R. F. Stebbings (2005), Charge transfer cross sections for energetic neutral atom data analysis, *J. Geophys. Res.*, *110*, A12213, doi:10.1029/2005JA011298.

Lundin, R., H. Borg, B. Hultqvist, A. Zakharov, and R. Pellinen (1989), First measurements of the ionospheric plasma escape from Mars, *Nature*, *341*, 609.

Ma, Y., A. F. Nagy, K. C. Hansen, D. L. DeZeeuw, and T. I. Gombosi (2002), Three-dimensional multispecies MHD studies of the solar wind interaction with Mars in the presence of crustal fields, *J. Geophys. Res.*, *107*(A10), 1282, doi:10.1029/2002JA009293.

Mura, A., et al. (2007), ENA detection in the dayside of Mars: ASPERA-3 NPD statistical study, *Planet. Space Sci.*, *56*, 840–845.

Nilsson, H., et al. (2006), Investigation of the influence of magnetic anomalies on ion distributions at Mars, *Space Sci. Rev.*, *126*, 355–372.

Wurz, P., A. Galli, S. Barabash, and A. Grigoriev (2008), Energetic neutral atoms from the heliosheath, *Astrophys. J.*, *683*, 248–254.

———————

S. Barabash, A. Ekenbäck, Y. Futaana, A. Grigoriev, and M. Holmström, Institutet för Rymdfysik, P.O. Box 812, SE-98128 Kiruna, Sweden.

M.-C. Fok, Geospace Physics Laboratory, NASA Goddard Space Flight Center, Code 673, Greenbelt, MD 20771, USA.

A. Galli and P. Wurz, Physikalisches Institut, University of Bern, Sidlerstrasse 5, CH-3012 Bern, Switzerland. (galli@space.unibe.ch; peter.wurz@space.unibe.ch)

H. Gunell, Department of Physics, West Virginia University, P.O. Box 6315, Morgantown, WV 26506, USA.

E. Kallio, Finnish Meteorological Institute, P.O. Box 503, FIN-00101 Helsinki, Finland.